

# Morphological Evolution of Zn-Sponge Electrodes Monitored by In Situ X-ray Computed Microtomography

Benedetto Bozzini,\* Claudio Mele, Alessio Veneziano, Nicola Sodini, Gabriele Lanzafame, Antonietta Taurino, and Lucia Mancini




Cite This: *ACS Appl. Energy Mater.* 2020, 3, 4931–4940



Read Online

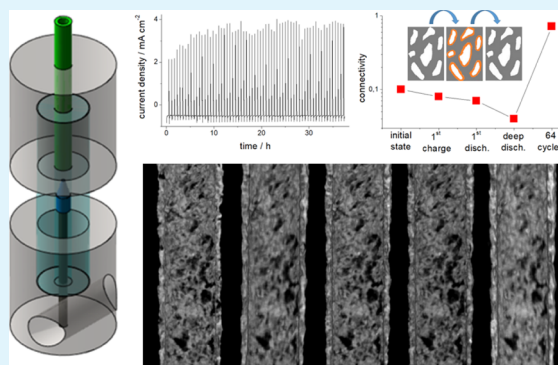
ACCESS |

 Metrics & More

 Article Recommendations

**ABSTRACT:** Use of Zn sponges has been recently proposed as an effective means of limiting the shape change and dendrite formation issues, affecting the anodes of electrically rechargeable Zn-based batteries. This paper contributes to this field of research with in situ X-ray computed microtomography (XCMT) monitoring of the morphological and chemical changes undergone by Zn-sponge anodes during electrochemical cycling. Starting from a pristine anode, fabricated in the discharged state, this was first charged and then subjected to a representative series of charge–discharge sequences and, in correspondence, it was studied by XCMT in order to determine (i) the volume fractions of Zn and ZnO, porosity, and their space arrangement and (ii) the degree of connectivity of the elemental Zn framework. Good stability of the metal framework, reversibility of the Zn and ZnO phases, and their space distribution, with a limited alteration of the pore structure, were observed over more than 60 charge–discharge cycles.

**KEYWORDS:** X-ray computed microtomography, in situ, zinc, battery, metal sponge, anode, zinc oxide



## 1. INTRODUCTION

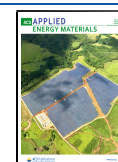
Rechargeable Zn-based batteries, in particular, with air electrodes, are promising candidates for next-generation energy storage because they offer higher specific energy, competitive cost, abundant raw-material resources, environmental friendliness, and better safety than most of the currently available competing technologies.<sup>1–5</sup> Although primary Zn–air batteries have been developed into widespread commercial devices since the mid 70s, successful applications of secondary Zn–air batteries are still hindered by various technical and economical hurdles. The most notable challenge is to improve their cycle life that is crucially affected by the choice and management of the air cathode, electrolyte, and Zn anode.<sup>6–8</sup> One of the main drawbacks, shared by all Zn-based battery chemistries, is the limited cycle life of the Zn electrode because of morphology changes upon cycling.<sup>9–13</sup> In order to cope with structural and morphological cycling instabilities of the Zn anode, several solutions have been proposed.<sup>14–19</sup> Among the most recent approaches, a highly promising one is that of Zn-sponge electrodes.<sup>20–27</sup> Their structure consists in a monolithic, porous architecture, exhibiting connected metallic Zn branches, covered with a layer of ZnO of thickness depending on the depth of discharge (DOD). The inner, connected core of electron-conductive metallic Zn branches is meant to persist even down to deep DODs, in principle allowing extensive

electrochemical cycling without the formation of macroscale dendrites or loose particles. In the present paper, we propose the use of in situ X-ray computed microtomography (XCMT) as an advanced research tool for the study of Zn-sponge electrodes. In the last decade, XCMT has progressively emerged as a powerful method to study batteries, in principle allowing nondestructive imaging of intact devices at any stage of their operational life, with in situ and in operando capabilities. XCMT enables analyses of the structure at scales ranging from below one micron to several millimeters, with the spatial resolution that anticorrelates with the probed sample volume. Pioneering XCMT studies addressed ZEBRA<sup>28</sup> and alkaline Zn<sup>29</sup> systems, while more recently, much work has been devoted to the more popular lithium-ion batteries (LIBs) (for an overview, see refs 30 and 31). Several aspects of LIB science and technology have been addressed by XCMT, covering scales from that of the whole cell (*ca.* 1 cm),<sup>32–37</sup> down to that of single particles of cathodic material (*ca.* 10

**Received:** March 6, 2020

**Accepted:** April 29, 2020

**Published:** April 29, 2020



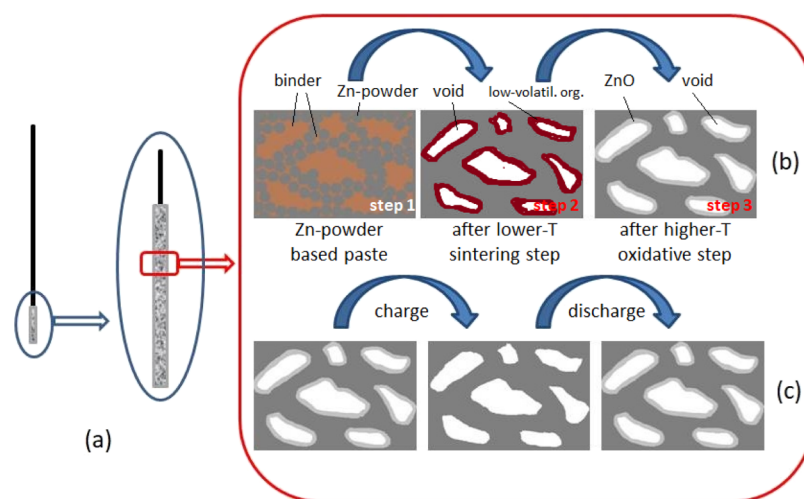


**Figure 1.** (a) Schematic representation of the graphite-supported Zn-sponge anode. (b) Cross-sectional sketch of the fabrication steps. (c) Structural changes corresponding to charge and discharge.

$\mu\text{m}$ ).<sup>38–41</sup> Moreover, dynamic studies have been performed of active material evolution<sup>42–44</sup> and degradation,<sup>45–47</sup> as well as thermal runaway.<sup>48</sup>

A close-knit group of mainly very recent publications has demonstrated that XCMT can provide powerful handles to gain insight into a range of materials science aspects of Zn-based batteries. Primary<sup>30</sup> and secondary<sup>49</sup> commercial Zn–MnO<sub>2</sub> alkaline batteries were investigated *in situ* at different DODs at the mesoscopic and full-cell scales. Manke *et al.*<sup>29</sup> used synchrotron-based XCMT to highlight the spatial and size distribution and oxidation progress of Zn particles and the swelling and breaking of cathodic MnO<sub>2</sub>, while Osenberg *et al.*<sup>49</sup> used laboratory-based XCMT to observe changes in three-dimensional (3D) morphology of the Zn anode and of the MnO<sub>2</sub> cathode<sup>50</sup> and<sup>51</sup> studied commercial button-cell zinc-air batteries (ZABs) with laboratory-based XCMT and used imaging results to validate multiphysics mathematical models of material evolution and cell voltage. ZABs were studied also in cells specifically designed for *in situ* XCMT.<sup>52–55</sup> Schröder *et al.*<sup>52</sup> carried out *in situ* laboratory-based XCMT analyses of a primary ZAB, with the main purpose of imaging the penetration of the electrolyte into the gas-diffusion layer, as a function of DOD. Franke-Lang *et al.*<sup>53</sup> and Christensen *et al.*<sup>54</sup> followed the cycling of secondary ZABs by *in situ* XCMT at the mesoscopic and millimeter scale. Reference 53 reports that cycling causes changes in morphology of Zn and air electrodes. Reference 54 combined *in situ* XCMT with X-ray diffraction to monitor the space- and time-dependent conversion of Zn and ZnO during cycling. Titscher *et al.*<sup>55</sup> followed, on the cell scale, the evolution of Zn and ZnO components. The anodic hopper and the air cathode of a Zn–air fuel cell were studied in ref 56 by laboratory-based XCMT. Finally, Yufit *et al.*<sup>57</sup> employed *in situ* synchrotron XCMT for a multiscale analysis of Zn dendrite formation.

Notwithstanding incipient, but intense interest in XCMT investigations of Zn batteries, it seems that this approach has not been attempted so far for *in situ* investigation of Zn-sponge electrodes. The only related publication is ref 27, which reports an *ex situ* XCMT characterization of two Zn-sponge samples, fabricated with different volume fractions of solid. In this work, the authors showed that higher-solid content materials exhibit

higher interconnectivity that, in turn, correlates with better electrochemical performance.

The study presented in this paper describes the first *in situ* XCMT analysis of the charge–discharge behavior of a Zn-sponge anode. The results of our investigation have enabled to gain positive dynamic information regarding the degree of connectivity of the metallic framework, the fractions of Zn and ZnO that are interconverted during cycling, and the porosity changes brought about by electrochemical operation. This approach, on the one hand, allows us to follow the morphochemical changes that are claimed to be the key to the success of this type of anode and, on the other hand, paves the way to knowledge-based and rational design of the operational protocols of Zn-sponge-based batteries.

## 2. EXPERIMENTAL SECTION

**2.1. Fabrication and Characterization of Zn Sponges.** The preparation of Zn sponges was inspired by the protocol detailed in ref 20 that was modified in view of fabricating Zn anodes for synchrotron-based *in situ* XCMT high-resolution imaging at the Zn K-edge. In fact, X-ray transmission experiments at these energies exhibit stringent thickness requirements that have to be coped with by specialized fabrication procedures. Even though the tomographic investigation described in the present paper was carried out with hard X-ray from a conventional high-voltage source and could have been carried out even with thicker anodes, our aim was to develop a flexible electrochemical cell for *in situ* XCMT that could be employed also for synchrotron-based measurements at lower energies, from a few keV up to a few tens of keV. Our equivalent bulk Zn thickness limit has been thus set to 400  $\mu\text{m}$ , specifically optimized for transmission of X-ray in the 30/35 keV range that ensures high chemical specificity for Zn-containing species. In order to fabricate Zn-sponge electrodes with these thickness characteristics, we applied the sponge-precursor paste onto an X-ray transparent current collector, consisting of a graphite rod, 500  $\mu\text{m}$  in diameter (Figure 1a). To this aim, a dense paste is required that cannot be obtained with the literature procedure, designed for casting into moulds.<sup>20–22,27</sup>

As hinted at in the Introduction section, the rationale of the metal-sponge preparation method is to fabricate a Zn anode initially in the discharged state, consisting of a continuous, ramified structure of metallic Zn, the branches of which are coated with a layer of ZnO. With this configuration, thin ZnO layers are efficiently contacted: electronically via the Zn core and ionically via the porosity of the spongy structure. Upon the first charge, a sizable fraction of the ZnO layer is converted to metallic Zn; and during discharge, an appropriate

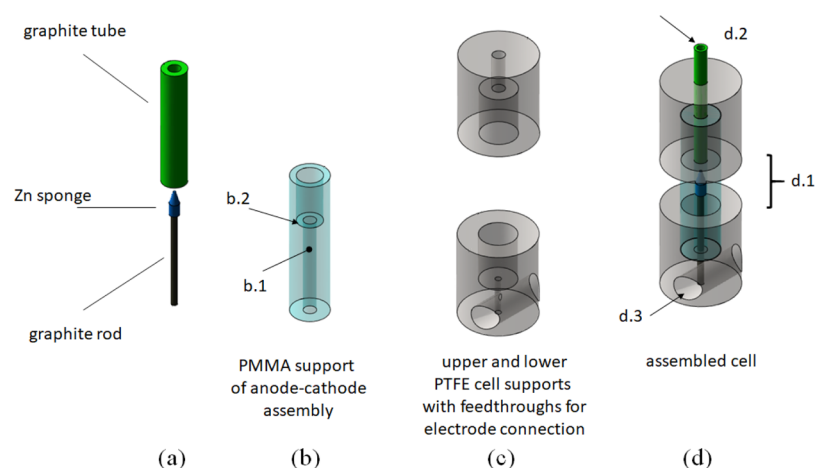


**Figure 2.** Scheme of the electrochemical cell developed for *in situ* XCMT. Conceptual drawings, not to scale. (a) Working and counter electrodes; (b) electrode support system; (c) cell support; and (d) assembled cell.

amount of the external, branched structure is converted back to ZnO, without oxidizing the core of the continuous metallic skeleton. The fabrication of this particular spongy structure goes through three steps, as sketched in Figure 1b: the first one consists in blending Zn powder and organic ingredients, and the next two are heat treatments (step 1, Figure 1b). The first step is the fabrication of the Zn-powder-based paste, containing appropriate organics that will lead to the formation of the spongy structure. The paste is then shaped into anodes of the required form. In ref 20, a fluid paste is prepared and cast into moulds; in the present work, instead, a thicker paste is produced, which can be easily formed into a freestanding object or spread onto a support, such as the graphite rods we used in this study. Even before heat treatment, the freestanding anode precursors and the coated graphite rods exhibit mechanical properties adequate for subsequent handling (step 2, Figure 1b). The shaping of anodes is followed by a second, sintering step in an inert atmosphere at a temperature slightly below the Zn melting point: in this step, on the one hand, the more volatile fraction of organics is removed, leaving behind a porous structure, while the less volatile binder-related species arrange on the surface of the pore cavities, and, on the other hand, Zn particles sinter forming a reticulated structure (step 3, Figure 1b). Finally, a third, oxidative heat-treatment step is carried out in air, at temperatures above the Zn melting point. In this step, the pore-templating residual organics are gradually removed and replaced by a ZnO layer that coats the sintered Zn skeleton, additionally forming a microtemplating mould in which molten Zn arranges into a tougher, branched structure with an appropriate degree of connectivity.

The paste-fabrication procedure consisted in (i) mixing 6 g of micrometric Zn powder (Todini and Co. S.p.a., Monza, Italy), 7 mg of sodium dodecyl sulfate (Panreac Applichem), and 0.21 g of carboxymethylcellulose (CTS) in a beaker and stirring for 8 min; (ii) adding 1 mL of ultrapure water under stirring until foam forms; and then (iii) adding 2.3 mL of *n*-pentane (Merck) still under stirring for about 10 more min, until the paste achieves a plastic and spreadable consistency.

The two types of samples that were prepared for this study are described below. (i) Cylindrical pellets, having similar geometry to that proposed in ref 20 (10 mm diameter and 10 mm height), were fabricated for electrochemical testing and for comparison with published data. The pellets were obtained by pressing the paste into moulds. (ii) Anodes for the XMCT cell were fabricated by spreading a layer of the Zn paste onto graphite rods (0.5 mm diameter, 60 mm length, Niji) and rolling it to the required final thickness of *ca.* 200  $\mu\text{m}$ . The as-formed pellets and anodes were heat-treated as described above, according to the procedure reported in ref 20. Briefly, the samples were transferred to a tube furnace (Materials Mates Italia S.r.l., Milan, Italy), heated under flowing Ar at 2  $^{\circ}\text{C min}^{-1}$  to 409  $^{\circ}\text{C}$ ,

and held at this temperature for 2 h. The tube was then opened to air, heated at 2  $^{\circ}\text{C min}^{-1}$  to 665  $^{\circ}\text{C}$ , and held at this temperature for 2 h. Finally, heat was turned off, and the samples were allowed to cool in the furnace down to room temperature. Finally, after heat treatment, a Celgard 3501 separator was applied to the graphite-supported anodes.

**2.2. Electrochemical Measurements.** Electrochemical measurements—consisting in anode charge and discharge experiments—were carried out with a VersaSTAT 3 potentiostat in a three-electrode configuration. Electrochemical impedance spectrometry (EIS) measurements were performed at an open circuit potential (OCP) by applying a potential sine-wave of amplitude 10 mV<sub>pp</sub> and scanning the frequency in the range 100 kHz to 1 mHz. For comparison with literature data, we tested the electrochemical response of the cylindrical Zn-sponge pellet electrodes to charge–discharge cycles. These experiments were carried out in a three-electrode cell, with the pellet used as the working electrode (WE), mounted in a hanging-meniscus configuration. A Pt wire was used as the counter electrode (CE), a Zn wire was used as the quasi-reference electrode (QRE), and the electrolyte was a 6 M KOH aqueous solution. The graphite-supported Zn-sponge anodes were subjected to similar charge–discharge cycles in a cell specifically developed for *in situ* XCMT characterization (details in Section 2.4).

**2.3. Electron Microscopy.** The morphology of the Zn-sponge anodes, after each of the fabrication steps, as well as after representative electrochemical cycling, was investigated by scanning electron microscopy (SEM). A Zeiss NVISION 40 machine, equipped with a high-resolution SEM Gemini column, was used. Secondary electron images were acquired by tuning the working conditions (electron beam energy and current) in order to limit charging effects due to either the incorporation of organic materials or Zn oxidation.

**2.4. Electrochemical Cell for In Situ XCMT Experiments.** The cell developed for *in situ* XCMT experiments is sketched in Figure 2. The electrodes, fabricated as described in Section 2.1, were positioned, as shown in Figure 2a. The CE is a graphite tube, 10 mm long, with an external diameter of *ca.* 2 mm and an internal diameter of 1 mm. The relative positioning of working and counter electrodes is ensured using a cylindrical PMMA support (Figure 2b, external diameter 3 mm, length 20 mm) that also acts as the X-ray optical window (as better specified in Figure 2d). In order to accurately define the electrode position, the graphite rod is inserted into a cylindrical hole and drilled into the PMMA support (b.1). Two O rings are placed into the smaller-diameter section of this hole (diameter 1 mm: the O rings are not shown in the image), on the one hand, to keep the electrode tightly in place without damaging it mechanically and, on the other hand, to act as a seal, preventing electrolyte leakage. The Zn sponge rests on the annular section, where the topmost O ring is located (b.2, in correspondence of the change in hole diameter from 1 to 2 mm for the PMMA support). The Zn

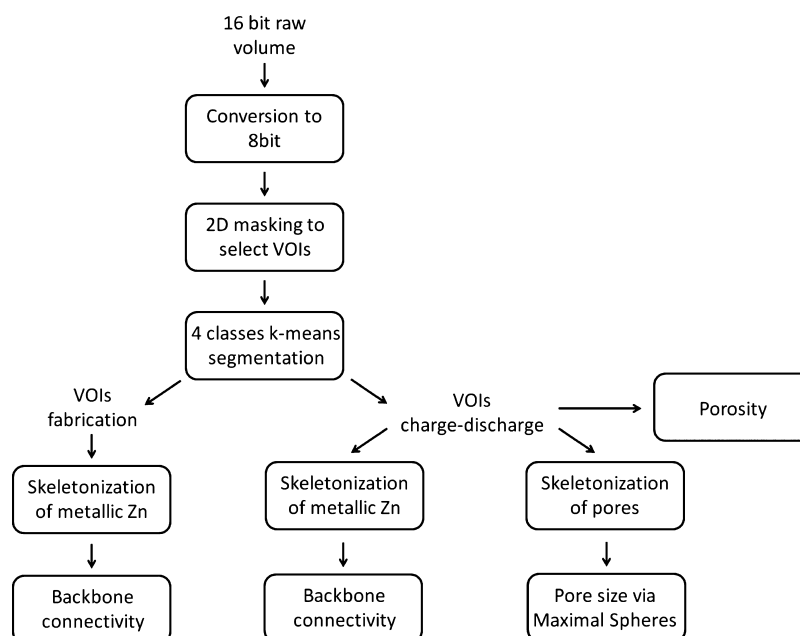


**Figure 3.** Protocol used for X-ray micro-CT processing and analysis of reconstructed volumes or selected volumes of interest (VOIs) of the anodes. Each step in the protocol was performed using the Pore3D software library custom-developed at Elettra.<sup>60</sup>

sponge is in contact with the upper O ring, thus minimizing the galvanic coupling between the Zn sponge and the uncoated section of the graphite rod. The same annular section (b.2) also supports the bottom of the graphite tube. The Zn-wire QRE is placed axially into the graphite tube from above, and it is kept in position with a plastic cap (not shown). The assembly of the components shown in Figure 2a,b is secured mechanically by two further supports—depicted in Figure 2c—that also ensure rugged electrical connections to the electrodes. The assembled cell is shown in Figure 2d. Here, the cylindrical X-ray window is the section indicated as (d.1). The cathode is directly connected to the external circuit, by soldering with Ag paste the top of the cylinder (d.2) to a Kapton-coated Cu wire, 0.2 mm in diameter. The electrical connection to the anode is obtained by placing a piece of the same Cu wire in the horizontal hole (d.3) and soldering it to the bottom of the graphite rod, again with the Ag paste.

**2.5. XCMT Measurements.** XCMT measurements were performed using the TomoLab station at the Elettra synchrotron facility in Basovizza (Trieste, Italy).<sup>58</sup> The instrument is equipped with a sealed microfocus X-ray source (L9181, Hamamatsu, Japan) and delivers a polychromatic beam in a voltage range of 40–130 kV, with a maximum current of 300  $\mu\text{A}$  and a minimum focal spot size of 5  $\mu\text{m}$ . The employed detector was a water-cooled, 12-bit, 4008  $\times$  2672 pixels CCD camera (XDI-VHR 60, Photonic Science, UK) characterized by a pixel size of 9  $\times$  9  $\mu\text{m}^2$ , customized by Photonic Science with a demagnifying optics system (1.38:1) giving an effective pixel size of 12.5  $\times$  12.5  $\mu\text{m}^2$ . The optical system has been coupled to a gadolinium oxysulphide scintillator screen, with a layer density of 15  $\text{mg cm}^{-2}$ . Thanks to the cone-beam geometry, it is possible to achieve a spatial resolution close to the focal spot size. It is well-known that a polychromatic beam from a microfocus X-ray generator allows us to reveal the phase jumps in a multiphase sample, if appropriate experimental conditions are applied.<sup>59</sup> At the TomoLab station, we were able to perform propagation-based phase-contrast XMCT measurements on our samples.

The cell was subjected, outside the TomoLab station, to the electrochemical treatment steps detailed in Section 3.2.3 and after each one of them, it was screwed in the center of the high-resolution rotation stage and subjected to the acquisition of a tomographic scan. We define this protocol *in situ*, according to the definition in ref 29. The imaging conditions adopted were voltage = 70 kV, current = 114  $\mu\text{A}$ , 0.5 mm-thick Al filter, exposure time/projection = 7.0 s, source-

to-sample distance = 80 mm, and source-to-detector distance = 400 mm. A 2  $\times$  2 binning was applied to the detector pixels, giving an effective pixel size of 5.0  $\mu\text{m}$ . For each scan, 1800 projections were recorded. Starting from the two-dimensional (2D) projections, a 3D volume was reconstructed using the commercial software COBRA (Exxim, USA) based on the Feldkamp algorithm,<sup>60</sup> which also allowed to correct beam-hardening artifacts. The reconstructed slices have been visualized using the open source Fiji software,<sup>61</sup> while 3D image renderings have been obtained with the commercial software VGStudio MAX 2.0 (Volume Graphics, Germany).

**2.6. Processing and Analysis of XMCT Data.** The X-ray images of the graphite-supported Zn-sponge anodes were processed and analyzed with the Pore3D software library custom-developed at Elettra.<sup>58,62</sup> As a preliminary step, the images were scaled over a 0/255 grayscale range and underwent ring artifact removal using the Sijbers and Postnov algorithm.<sup>63</sup> Masking operations were necessary to select only the region of the images occupied by the sample, thus excluding the background. Two-dimensional masking was applied to individual images, using the following procedure: the application of an automatic Otsu thresholding<sup>64</sup> provided the first estimation of the position and shape of the region of interest in the images, while following iterations of dilation and erosion processing operators<sup>65</sup> filled the whole region of the Zn-sponge anodes. Then, a unique value was assigned to the identified background, in order to separate it from the region of interest. The masked images underwent segmentation to differentiate the pores and the metallic Zn from ZnO. Because of the multiphase composition of Zn-sponge anodes, the images were segmented using the k-means clustering algorithm,<sup>66</sup> selecting four classes, and the class corresponding to pores and metallic Zn was isolated. Pores and metallic Zn represented by less than 3 voxels in the volume were not taken into account in the subsequent analyses. The porosity of Zn anodes and the distribution of metallic Zn were then analyzed throughout the charge–discharge experiment.

The quantity and distribution of metallic Zn at each step of the anode fabrication and the charge–discharge sequence were assessed using the *Backbone* connectivity approach.<sup>67</sup> The backbones of a 3D structure are portions of the elements of which are all connected to each other. Each individual backbone is separated from the other ones. The number of backbones within the 3D structure is related to the interconnectivity of the material under analysis. In the case of the anodes, the number of backbones was measured to quantify the connectivity of the metallic Zn phase. In fact, the higher the number

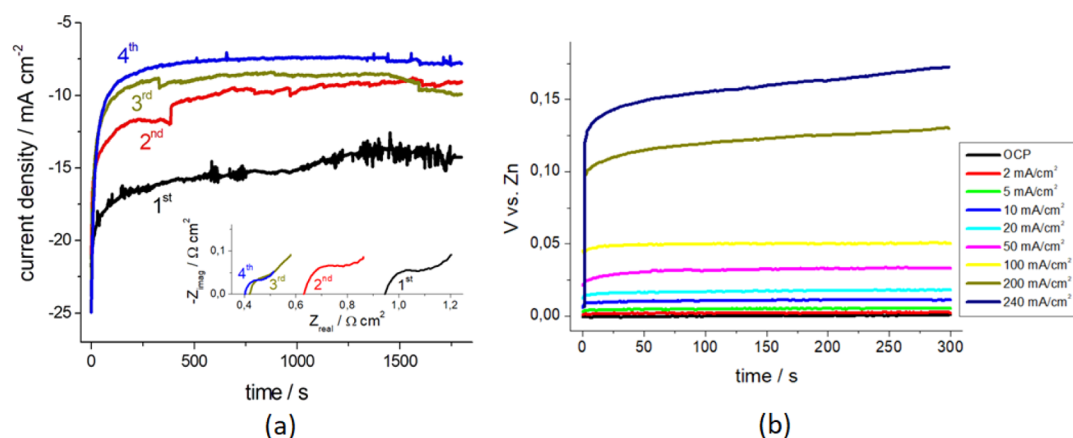


**Figure 4.** (a) Potentiostatic charge plots at  $-50\text{ mV}_{\text{Zn}}$  for the as-fabricated Zn-sponge pellet in a 6 M KOH solution. Current density refers to the nominal geometric pellet area, exposed to the electrolyte. Inset: EIS plots recorded after each potentiostatic charge step. (b) Anodic galvanostatic discharge voltage of the precharged Zn-sponge pellet in a 6 M KOH solution.

of backbones, the less interconnected is the overall metallic Zn framework. Growth in backbone connectivity would thus indicate the increased formation of metallic Zn. To quantify connectivity, the segmented metallic Zn was skeletonized<sup>68</sup> through an image-processing operation that reduces the morphology of a 3D digital object to a network of nodes and branches that preserves the geometric and morphological features of the original object.<sup>62,68</sup> For this operation, we used the LKC skeleton algorithm.<sup>69</sup> The connected components of the skeleton were calculated, to identify each isolated backbone. The connectivity parameter was then calculated as the ratio between the volume of the largest backbone and the volume of all metallic Zn.<sup>67</sup>

To capture the morphological variations along the charge–discharge experimental series, we also measured the fraction and size of pores. The fractional porosity was measured as the proportion between the volume occupied by the segmented pores and the total volume of the Zn-sponge anode: a quantity ranging from zero to one. The pore size was extracted using the *SkeletonAnalysis module* of Pore3D. First, the 3D volume of segmented pores underwent skeletonization,<sup>68,69</sup> followed by the application of the *Maximal Spheres* method.<sup>70</sup> In this method, the diameter of the maximal sphere enclosed within a pore is calculated and then used as the pore size. The obtained pore size distribution was fitted with a log-normal distribution, whence mean pore sizes and their standard deviations were estimated.

The protocol used for the analysis of XMCT images and selected VOIs of the anodes is schematized in Figure 3.

### 3. RESULTS AND DISCUSSION

**3.1. Characterization of Zn-Sponge Pellets.** Because Zn-sponge anodes are fabricated in the discharged state, we tested their response to the first charge, by applying a sequence of potentiostatic steps of 30 min at  $-50\text{ mV}$  versus Zn QRE (henceforward referred to as  $\text{mV}_{\text{Zn}}$ ). In correspondence of each charge step, we observed a decrease in the circulating current, indicating a progressive reduction of ZnO to Zn (Figure 4a). EIS measurements have been also performed after each potentiostatic charge step in order to monitor the decrease in the ohmic resistance of the pellet, denoting the progress of charging: the results are reported in the inset of Figure 4a and show a variation from  $0.95$  to  $0.40\ \Omega\ \text{cm}^2$ , coherently with a progressive reduction of ZnO to Zn in the branched structure of the sponge electrode. Furthermore, the OCP of the Zn sponge, measured after the fourth step, shows a value very close to that of the metallic Zn QRE:  $7.7 \pm 0.4\text{ mV}$ .

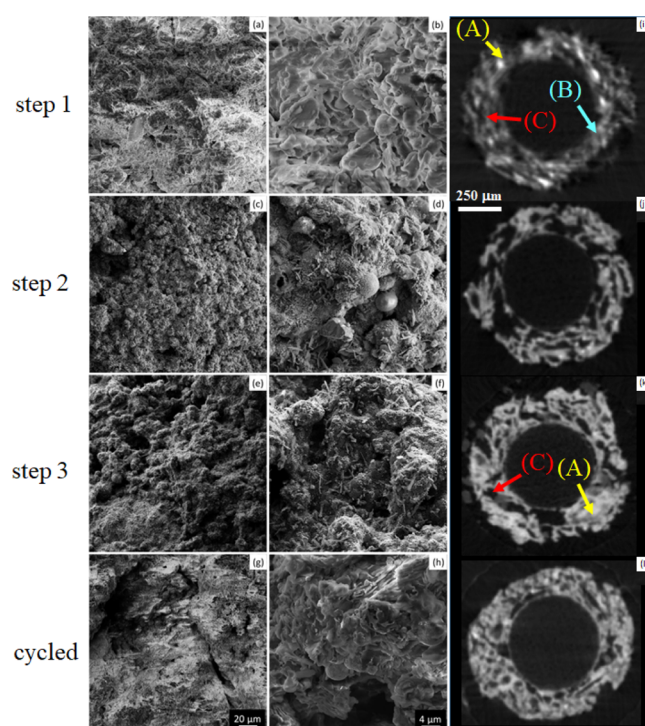


**Figure 5.** Field emission scanning electron microscopy (FE-SEM) micrographs of the graphite-supported Zn-sponge anode: the as-fabricated sample (step 1),  $1000\times$  (a) and  $5000\times$  (b); the sample that has undergone only the first heat-treatment step ( $409\text{ }^\circ\text{C}$  in  $\text{N}_2$ , step 2),  $1000\times$  (c) and  $5000\times$  (d); the sample that has undergone the whole heat-treatment sequence (step 3),  $1000\times$  (e) and  $3000\times$  (f); and the electrochemically cycled sample (see Section 3.2.2 for details),  $1000\times$  (g) and  $3000\times$  (h). At the right of the SEM images (Panels i–l), for reference, we report reconstructed XCMT axial slices of the same materials, showing (A) metallic Zn, (B) binder, and (C) pores: in step 3, the pores are partially filled with ZnO and the cycled sample exhibits some degrees of pore closure.

In Figure 4b, we report galvanostatic discharge measurements of the Zn-sponge pellet electrode, precharged as described above, performed with the protocol proposed in ref 20. As the applied current density is increased from 2 to  $240\text{ mA cm}^{-2}$ , the overpotential remains below  $+200\text{ mV}$ : this low polarization falls well below the  $500\text{ mV}$  voltage drop,

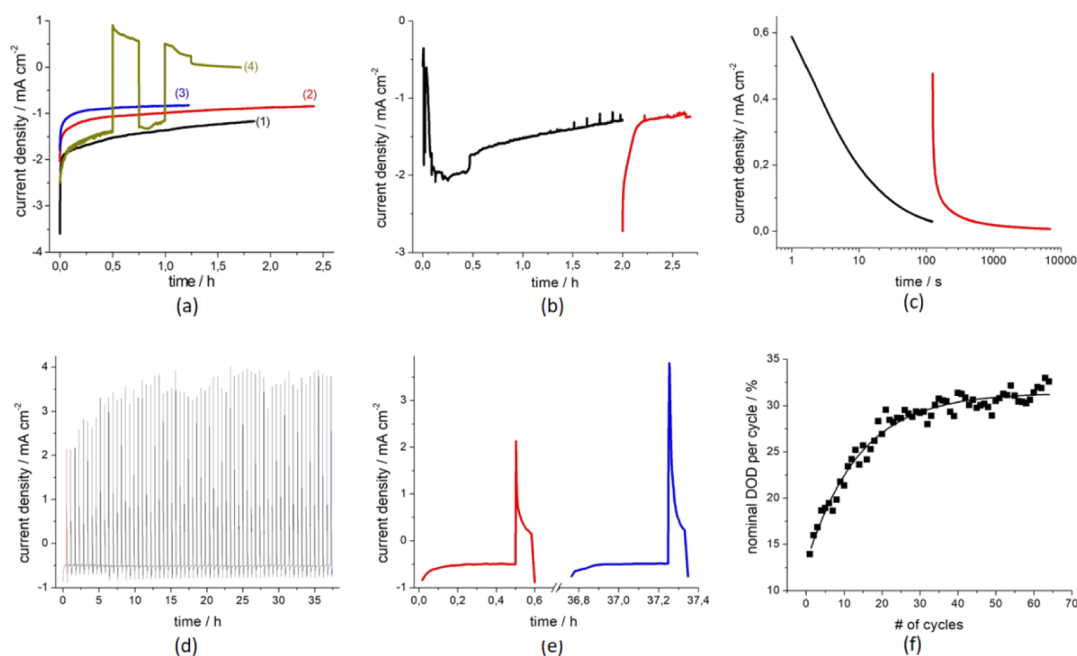


**Figure 6.** (a–e) Current density vs time traces for potentiostatic charge–discharge sequences of graphite-supported Zn-sponge anodes in 6 M KOH solution ( $\pm 50$  mV<sub>Zn</sub>, unless otherwise stated). (a) Electrochemical tests carried out without in-line imaging. (1–3) Sequential charge periods and (4) charge–discharge sequence. (b–f) Electrochemical measurements for *in situ* XCOMT. (b) Initial charge of the pristine sample. (c) Deep discharge at 1200 and 1300 mV<sub>Zn</sub>. (d) 64 charge–discharge cycles ( $-50/+500$  mV<sub>Zn</sub>). (e) Magnified 1st and 64th cycle from Panel (d). (f) Nominal DODs per cycle, referring to the data of Panel (d) (the continuous line is a guide for the eye).

**Table 1. Sample Description and Volumetric Data Details of the Investigated Electrochemical Cycling Conditions**

sample status	isotropic voxel size ( $\mu\text{m}$ )	analyzed volume (pixels <sup>3</sup> )	electrochemical conditions
initial state	5.0	164 × 151 × 935	pristine sample at OCP
charge	5.0	160 × 155 × 937	the anode is reduced by applying two subsequent potentiostatic steps
discharge	5.0	161 × 155 × 936	the anode is discharged by short-circuiting the cell for 2 h
deep discharge	5.0	165 × 151 × 937	the anode undergoes deep discharge by applying potentiostatic polarization at 1200 mV for 2 min and at 1300 mV for 2 h
after 64 cycles	5.0	172 × 152 × 935	a sequence of 64 charge–discharge cycles was applied, 30 min at $-50$ mV and 5 min at $+500$ mV

tolerated in conventional Zn-containing batteries, including Zn–air ones (e.g., ref 12). A similar behavior was obtained with a Zn sponge in a flooded half-cell configuration.<sup>20</sup> The ability of this electrode to sustain such low polarizations at very high current demands—confirmed by our results—arises from the fact that the inherently fast electrode reaction for the Zn<sup>0</sup>/Zn<sup>2+</sup> electrode redox reaction is not appreciably hindered by passivation or mass-transport contributions.

**3.2. Characterization of the Graphite-Supported Zn-Sponge Anodes.** **3.2.1. Microscopic Characterization.** In Figure 5, field emission scanning electron microscopy (FE-SEM) micrographs of graphite-supported Zn-sponge anodes are reported. The morphology of samples before heat treatment (Figure 5a,b) is, of course, characterized by individual flakes/grains, corresponding to the Zn-powder precursor, combined with the organic gelling agent and surfactant: as expected, the sample is very poorly electronically conducting, as evidenced by the strong sample charging under the electron beam. Figure 5c,d shows the images of a sample subjected only to the first heat-treatment step (i.e., 409 °C in N<sub>2</sub>).

Spheroidized metal grains dominate the morphology, agglomerating in a form that leaves behind a polydisperse porosity. The globular features, resulting from heat treatment

of the original Zn powder at a temperature slightly below its melting point ( $T_M = 420$  °C), exhibit a limited degree of neck formation, still far from the desired branched structure. The sample that had undergone also the second heat-treatment step (665 °C in air) but has not yet been electrochemically cycled, presents the desired fibrous/branched structures (Figure 5e,f). These branched structures retain traces of the globular crystallites, characteristic of the first heat-treatment step, in the form of a humpy pattern that can be noticed along the branches. The surface of the branches is decorated with a mixture of sub-micrometric equiaxed and rod-shaped oxide crystallites, exhibiting the characteristic hexagonal morphology. Figure 5g,h, discussed in detail below in Section 3.2.2, presents the morphology of the heat-treated and electrochemically cycled sample.

**3.2.2. Electrochemical Characterization.** The electrochemical performance of the first batch of graphite-supported Zn-sponge electrodes was tested with charge and discharge sequences in the cell that was later used for tomography, without subjecting them to in-line imaging. In this context, we have quantified discharge in terms of a “nominal DOD”, defined as the ratio of the electrical charge (time integral of current) extracted during a given discharge step, to the charge (again, time integral of current) consumed during the charge

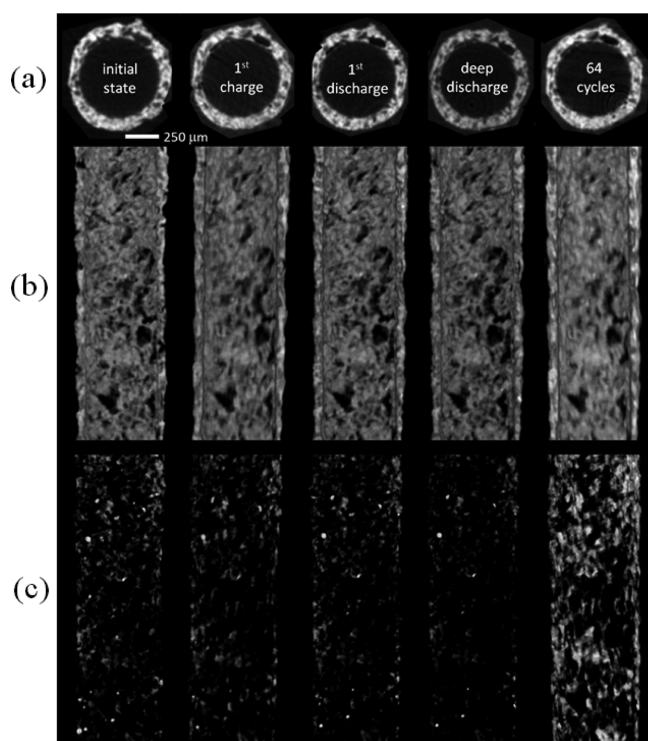


**Figure 7.** *In situ* XCMT. (a) Reconstructed axial slices, (b,c) volume renderings of graphite-supported Zn-sponge anodes under different electrochemical conditions: (i) initial state: as-fabricated, in the discharged state, at OCP; (ii) after first charge (see Figure 6b); (iii) after first discharge; (iv) after deep discharge (see Figure 6c); and (v) after 64 charge–discharge cycles (see Figure 6d). Voxel size:  $5 \mu\text{m}^3$ . The volume renderings of Panel (c) represent the Zn backbone connectivity for the same electrochemical conditions (see also Section 2.6 and Figure 8d).

step. The rationale underlying this definition is that we are endeavoring to oxidize only the fraction of Zn that has been reduced during the first electrochemical step following heat treatment, without consuming the metallic skeleton present in the as-fabricated sample. In Figure 6a, we report the current–time plots for three subsequent charging periods [plots (1–3)]. The conversion of a notable fraction of the ZnO shell to metallic Zn could be followed by monitoring the OCP values after each reduction period:  $1245.6 \pm 0.5$ ,  $505.8 \pm 0.5$ , and  $70.4 \pm 0.6 \text{ mV}_{\text{Zn}}$ . After charging, the cell was discharged by keeping it short-circuited overnight, and this resulted in essentially complete reoxidation of Zn, leading to a final OCP of  $1241.9 \pm 0.7 \text{ mV}_{\text{Zn}}$ . After this deep discharge, the cell was subjected to a sequence of two charge–discharge steps [plot (4) of Figure 6a: discharges to nominal DODs per cycle of ca. 20 and 10%]. The SEM micrographs (Figure 5g,h) and the XCMT axial slice (Figure 5l) of the sample subjected to these cycling tests show that mesoscopic agglomerates have formed, covered by a rather compact oxide layer, characterized by stacking of bunches of crystal-plane steps of micrometric height. Notwithstanding some degrees of compaction of the material, the high-residual porosity witnesses a sound morphological stability.

**3.2.3. *In Situ* XCMT Measurements.** *In situ* XCMT experiments were carried out with the following electrochemical protocol. After having measured a scan with the pristine sample at OCP (initial state), we have reduced the material by applying two subsequent potentiostatic steps (1st

charge). Figure 6–e displays the current density versus time traces of the *in situ* experiments. Figure 6b reports the initial charging transient, in correspondence of which the OCP changed from  $1135.1 \pm 12.9$  to  $90.3 \pm 15.0 \text{ mV}_{\text{Zn}}$ . After initial charging, the electrode was discharged by short circuiting the cell for 2 h: the final OCP was  $1083.8 \pm 6.4 \text{ mV}_{\text{Zn}}$ . Then, the Zn-sponge electrode was subjected to a deep discharge, consisting in potentiostatic polarization at  $1200 \text{ mV}_{\text{Zn}}$  for 2 min and at  $1300 \text{ mV}_{\text{Zn}}$  for ca. 2 h (Figure 6c): the final OCP was  $1255.2 \pm 6.9 \text{ mV}_{\text{Zn}}$ . Finally, after deep discharge, a sequence of 64 charge–discharge cycles was applied (30 min at  $-50 \text{ mV}_{\text{Zn}}$  and 5 min at  $+500 \text{ mV}_{\text{Zn}}$ ; Figure 6d,e). The sequence of electrochemical conditions to which the imaged anode has been subjected is summarized in Table 1, together with information regarding data acquisition. XMCT images of *in situ* observations of the evolution of a Zn-sponge anode are shown in Figure 7, and morphological descriptors extracted from them (for details, see Section 2.5) are plotted in Figure 8.

As detailed above, the anode is fabricated in the discharged state, whereby a relatively thick ZnO layer covers the continuous metallic Zn network with relatively thin branches. After the initial charging step, metal-like contrast (white) increases, while oxide-like contrast (grey) decreases. In correspondence, the degree of connectivity (Figure 8d) is essentially the same, while the arrangement of pores changes shape, the porosity fraction increases (Figure 8a), and the pore size decreases (Figure 8c). The porosity increase and pore size decrease can be explained, respectively, with the volume contraction of ZnO, resulting from transformation into Zn and the shrinking of Zn-rich zones, leading to the opening of small pores.

After the first discharge, a type of contrast more similar to that of the initial state is regained, owing to the relative increase in ZnO. Nevertheless, irreversible material transformations, due to the expansion of Zn during oxidation, lead to small changes in porosity arrangement and pore dimensions that do not affect measurably the connectivity of the metallic framework. After the deep discharge, oxide-type contrast (gray) predominates and, again, small changes in porosity distribution are observed, accompanied by a sizable decrease in connectivity. Finally, after 64 charge–discharge cycles, the axial and sagittal reconstructions are dominated by metal-like contrast (white) and a notable increase in connectivity is observed. This can be explained with the fact that the nominal DOD per cycle (Figure 6f) is rather low, and metallic Zn tends to accumulate during cycling: in correspondence, a slight tendency toward pore closure can be noticed.

## 4. CONCLUSIONS

Electrically rechargeable Zn-based batteries are highly prospective electrochemical energy storage devices for both mobile and stationary applications, but unsatisfactory anode stability upon cycling still impedes their practical application. Among the attempts to overcome Zn shape-change issues, the recently proposed approach based on Zn-sponge anodes seems very promising.<sup>20–24,27</sup> Research in the field is quite advanced and has achieved notable results regarding material fabrication capabilities and control of their electrochemistry, but *in situ* observations of these electrodes are still lacking and could contribute so far unavailable information for a more insightful mechanistic understanding leading to further performance improvement. This paper proposes the use of *in situ* XCMT to follow and quantify changes in shape and distribution of Zn

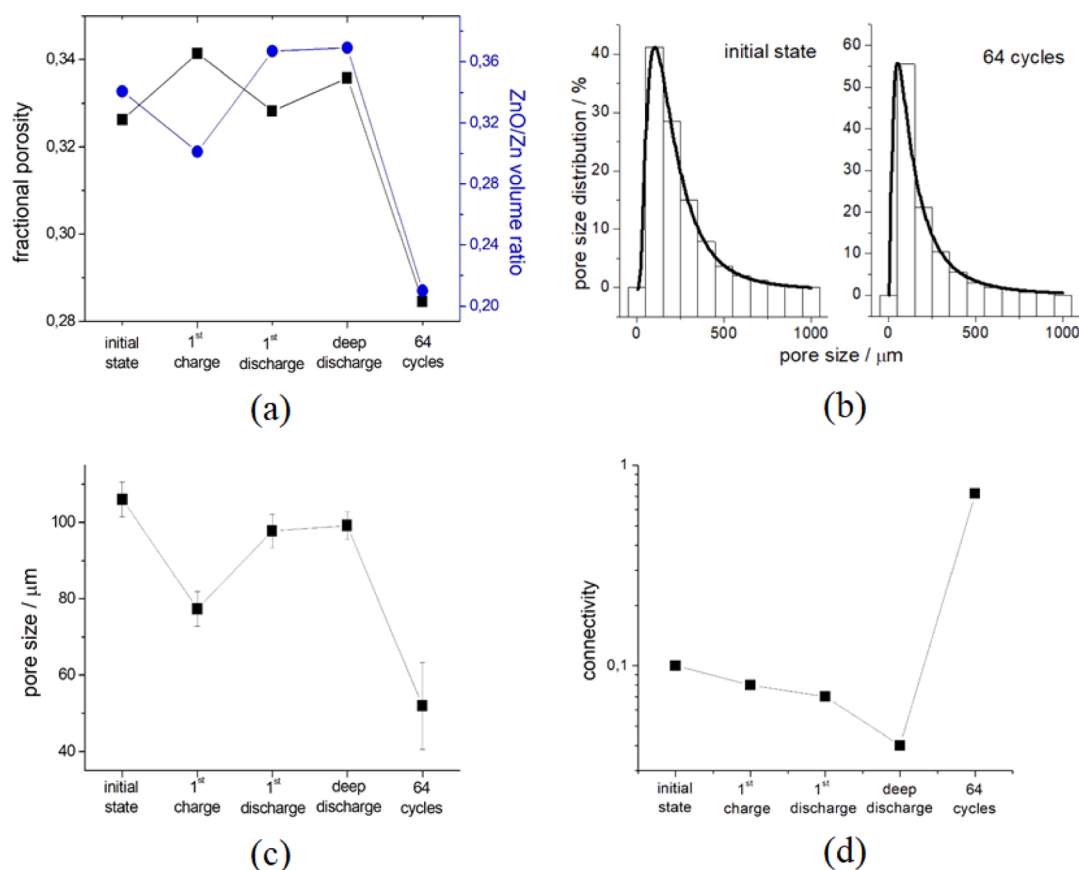


**Figure 8.** Morphological descriptors extracted from *in situ* XCOMT reconstructions. (a) Fractional porosity (fraction of the total anode volume occupied by pores) and ZnO/Zn volume ratio (ratio of the fractions of the total anode volume occupied by ZnO and Zn, respectively). (b) Representative pore size distributions and their log-normal fits: initial state and after 64 cycles. (c) Mean pore size and their standard deviations from log-normal fitting of pore size distributions. (d) Connectivity measured on the metallic Zn backbone during charge–discharge cycling. The backbones are identified using *SkeletonAnalysis* module in the Pore3D software library. Connectivity is measured as the ratio between the largest backbone and the volume of all backbones.

and ZnO phases, as well as porosity and connectivity of the metallic framework, during electrochemical cycling.

XCOMT requires special solutions in terms of maximum allowed metal thickness and cell geometry that we have tackled in order to develop a flexible tool with real-battery materials and realistic current-density distribution. Moreover, we have improved the Zn-sponge fabrication protocol, with respect to the state of the art, in order to cope with radiation-absorption constraints. Beyond its appropriateness for tomography experiments, the new fabrication procedure allows us to produce freestanding anodes of precisely controlled thickness, thus overcoming the limitations of the conventional paste-casting operation.

Our XCOMT tests have concentrated on the initial charging of an anode fabricated in the discharged state and on subsequent cycling in modes representative of extensive cycling and deep discharge. Reconstructed volumes, analyzed with appropriate image-processing methods, allowed us to follow, as a function of electrochemical operation, the relative variations of metal and oxide contents and their distribution, as well as the evolution of porosity, metal agglomeration, and metal connectivity. The metal-to-oxide ratio, framework porosity, and continuity, as well as the pore distribution, are affected by shrinking and expansion of the external shell of the sponge network, resulting from the alteration of oxidation and reduction processes, but they are quite reversible and only

prolonged cycling to limited DODs leads to a tendential increase in metal content and connectivity, accompanied by some degrees of pore closure.

In conclusion, with this work, we have proved that the application of X-ray microfocus tomography in the propagation-based phase-contrast mode gives direct access to morphochemical properties of Zn-sponge anodes, induced by working conditions and ageing. The availability of this information will enable knowledge-based material and cell design, as well as the definition of optimal charge–discharge policies.

## AUTHOR INFORMATION

### Corresponding Author

**Benedetto Bozzini** – Department of Energy, Politecnico di Milano, 20156 Milano, Italy; [orcid.org/0000-0002-2725-9157](https://orcid.org/0000-0002-2725-9157); Email: [benedetto.bozzini@polimi.it](mailto:benedetto.bozzini@polimi.it)

### Authors

**Claudio Mele** – Dipartimento di Ingegneria dell'Innovazione, Università del Salento, 73100 Lecce, Italy

**Alessio Veneziano** – Elettra—Sinicrotrone Trieste S.C.p.A., 34149 Trieste-Basovizza, Italy

**Nicola Sodini** – Elettra—Sinicrotrone Trieste S.C.p.A., 34149 Trieste-Basovizza, Italy



Gabriele Lanzafame – Elettra—Sinotrone Trieste S.C.p.A., 34149 Trieste-Basovizza, Italy

Antonietta Taurino – Institute for Microelectronics and Microsystems, IMM-CNR, 73100 Lecce, Italy

Lucia Mancini – Elettra—Sinotrone Trieste S.C.p.A., 34149 Trieste-Basovizza, Italy; LINXS—Lund Institute for Advanced Neutron and X-ray Science, 223 70 Lund, Sweden

Complete contact information is available at:  
<https://pubs.acs.org/10.1021/acsaem.0c00489>

## Notes

The authors declare no competing financial interest.

## REFERENCES

- (1) Li, Y.; Dai, H. Recent advances in zinc-air batteries. *Chem. Soc. Rev.* **2014**, *43*, 5257.
- (2) Lee, J.-S.; Tai Kim, S.; Cao, R.; Choi, N.-S.; Liu, M.; Lee, K. T.; Cho, J. Metal–Air Batteries with High Energy Density: Li–Air versus Zn–Air. *Adv. Energy Mater.* **2011**, *1*, 34.
- (3) Sapkota, P.; Kim, H. Zinc–air fuel cell, a potential candidate for alternative energy. *J. Ind. Eng. Chem.* **2009**, *15*, 445.
- (4) Haas, O.; Van Wesemael, J. Zinc–Air: Electrical Recharge. In *Encyclopedia of Electrochemical Power Sources*; Dyer, C. K., Mosley, P. T., Ogumi, Z., Rand, D. A. J., Scrosati, B., Eds.; Elsevier: New York, 2009; pp 384–392.
- (5) Mele, C.; Bozzini, B. Spectroelectrochemical investigation of the anodic and cathodic behaviour of zinc in 5.3 M KOH. *J. Appl. Electrochem.* **2015**, *45*, 43.
- (6) Xu, M.; Ivey, D. G.; Xie, Z.; Qu, W. Rechargeable Zn-air batteries: Progress in electrolyte development and cell configuration advancement. *J. Power Sources* **2015**, *283*, 358.
- (7) Pei, P.; Wang, K.; Ma, Z. Technologies for extending zinc–air battery's cyclife: A review. *Appl. Energy* **2014**, *128*, 315.
- (8) Gu, P.; Zheng, M.; Zhao, Q.; Xiao, X.; Xue, H.; Pang, H. Rechargeable zinc–air batteries: a promising way to green energy. *J. Mater. Chem. A* **2017**, *5*, 7651.
- (9) Lee, S.-H.; Jeong, Y.-J.; Lim, S.-H.; Lee, E.-A.; Yi, C.-W.; Kim, K. The stable rechargeability of secondary Zn-air batteries: is it possible to recharge a Zn-air battery? *J. Korean Electrochem. Soc.* **2010**, *13*, 45.
- (10) Kraytsberg, A.; Ein-Eli, Y. The impact of nano-scaled materials on advanced metal–air battery systems. *Nano Energy* **2013**, *2*, 468.
- (11) Zhang, X. G. Secondary batteries – Zinc System. In *Encyclopedia of Electrochemical Power Sources*; Dyer, C. K., Mosley, P. T., Ogumi, Z., Rand, D. A. J., Scrosati, B., Eds.; Elsevier: New York, 2009; pp 454–468.
- (12) Linden, D. Basic concepts. In *Handbook of Batteries*, 3rd ed.; Linden, D., Reddy, T. B., Eds.; McGraw Hill: New York, 2001; p 1200.
- (13) Turney, D. E.; Gallaway, J. W.; Yadav, G. G.; Ramirez, R.; Nyce, M.; Banerjee, S.; Chen-Wiegart, Y.-c. K.; Wang, J.; D'Ambrose, M. J.; Kolhekar, S.; Huang, J.; Wei, X. Rechargeable Zinc Alkaline Anodes for Long-Cycle Energy Storage. *Chem. Mater.* **2017**, *29*, 4819.
- (14) Caramia, V.; Bozzini, B. Materials science aspects of zinc–air batteries: a review. *Mater. Renew. Sustain. Energy* **2014**, *3*, 28.
- (15) Zhang, X. G. Fibrous zinc anodes for high power batteries. *J. Power Sources* **2006**, *163*, 591.
- (16) Drillet, J. F.; Adam, M.; Barg, S.; Herter, A.; Koch, D.; Schmidt, V.; Wilhel, M. Development of a Novel Zinc/Air Fuel Cell with a Zn Foam Anode, a PVA/KOH Membrane and a MnO<sub>2</sub>/SiOC-Based Air Cathode. *ECS Trans.* **2010**, *28*, 13.
- (17) Mele, C.; Bilotta, A.; Bocchetta, P.; Bozzini, B. Characterization of the particulate anode of a laboratory flow Zn-air fuel cell. *J. Appl. Electrochem.* **2017**, *47*, 877.
- (18) Chamoun, M.; Hertzberg, B. J.; Gupta, T.; Davies, D.; Bhadra, S.; Van Tassell, B.; Erdonmez, C.; Steingart, D. A. Hyper-Dendritic Nanoporous Zinc Foam Anodes. *NPG Asia Mater.* **2015**, *7*, No. e178.
- (19) Yan, Z.; Wang, E.; Jiang, L.; Sun, G. Superior cycling stability and high rate capability of three-dimensional Zn/Cu foam electrodes for zinc-based alkaline batteries. *RSC Adv.* **2015**, *5*, 83781.
- (20) Parker, J. F.; Chervin, C. N.; Nelson, E. S.; Rolison, D. R.; Long, J. W. Wiring zinc in three dimensions re-writes battery performance-dendrite-free cycling. *Energy Environ. Sci.* **2014**, *7*, 1117.
- (21) Parker, J. F.; Nelson, E. S.; Wattendorf, M. D.; Chervin, C. N.; Long, J. W.; Rolison, D. R. Retaining the 3D Framework of Zinc Sponge Anodes upon Deep Discharge in Zn–Air Cells. *Appl. Mater. Interfaces* **2014**, *6*, 19471.
- (22) Parker, J. F.; Chervin, C. N.; Pala, I. R.; Machler, M.; Burz, M. F.; Long, J. W.; Rolison, D. R. Rechargeable nickel–3D zinc batteries: An energy-dense, safer alternative to lithium-ion. *Science* **2017**, *356*, 415.
- (23) Jacoby, M. Zinc sponge protects rechargeable battery. *C&EN Global Enterprise* **2017**, *95*, 7.
- (24) Garino, N.; Lamberti, A.; Gazia, R.; Chiodoni, A.; Gerbaldi, C. Cycling behaviour of sponge-like nanostructured ZnO as thin-film Li-ion battery anodes. *J. Alloys Compd.* **2014**, *615*, S454.
- (25) Lu, W.; Xie, C.; Zhang, H.; Li, X. Inhibition of Zinc Dendrite Growth in Zinc-Based Batteries. *ChemSusChem* **2018**, *11*, 3996.
- (26) Stock, D.; Dongmo, S.; Miyazaki, K.; Abe, T.; Janek, J.; Schröder, D. Towards zinc-oxygen batteries with enhanced cycling stability: The benefit of anion-exchange ionomer for zinc sponge anodes. *J. Power Sources* **2018**, *395*, 195.
- (27) Ko, J. S.; Geltmacher, A. B.; Hopkins, B. J.; Rolison, D. R.; Long, J. W.; Parker, J. F. Robust 3D Zn Sponges Enable High-Power, Energy-Dense Alkaline Batteries. *ACS Appl. Energy Mater.* **2019**, *2*, 212.
- (28) Steinbock, L.; Dustmann, C.-H. Investigation of the inner structures of ZEBRA cells with a microtomograph. *J. Electrochem. Soc.* **2001**, *148*, A132.
- (29) Manke, I.; Banhart, J.; Haibel, A.; Rack, A.; Zabler, S.; Kardjilov, N.; Hilger, A.; Melzer, A.; Riesemeier, H. In situ investigation of the discharge of alkaline Zn–MnO<sub>2</sub> batteries with synchrotron x-ray and neutron tomographies. *Appl. Phys. Lett.* **2007**, *90*, 214102.
- (30) Pietsch, P.; Wood, V. X-Ray Tomography for Lithium Ion Battery Research: A Practical Guide. *Annu. Rev. Mater. Res.* **2017**, *47*, 451.
- (31) Wood, V. X-ray tomography for battery research and development. *Nat. Rev. Mater.* **2018**, *3*, 293.
- (32) Waldmann, T.; Iturrondobeitia, A.; Kasper, M.; Ghanbari, N.; Aguesse, F.; Bekaert, E.; Daniel, L.; Genies, S.; Gordon, I. J.; Löble, M. W.; De Vito, E.; Wohlfahrt-Mehrens, M. Review-Post-Mortem Analysis of Aged Lithium-Ion Batteries: Disassembly Methodology and Physico-Chemical Analysis Techniques. *J. Electrochem. Soc.* **2016**, *163*, A2149.
- (33) Shearing, P. R.; Howard, L. E.; Jørgensen, P. S.; Brandon, N. P.; Harris, S. J. Characterization of the 3-dimensional microstructure of a graphite negative electrode from a Li-ion battery. *Electrochem. Commun.* **2010**, *12*, 374.
- (34) Harris, S. J.; Lu, P. Effects of inhomogeneities – nanoscale to mesoscale – on the durability of Li-ion batteries. *J. Phys. Chem. C* **2013**, *117*, 6481.
- (35) Ziesche, R. F.; Arlt, T.; Finegan, D. P.; Heenan, T. M. M.; Tenggattini, A.; Baum, D.; Kardjilov, N.; Markötter, H.; Manke, I.; Kockelmann, W.; Brett, D. J. L.; Shearing, P. R. 4D imaging of lithium-batteries using correlative neutron and X-ray tomography with a virtual unrolling technique. *Nat. Commun.* **2020**, *11*, 777.
- (36) Finegan, D. P.; Scheel, M.; Robinson, J. B.; Tjaden, B.; Hunt, I.; Mason, T. J.; Millichamp, J.; Di Michiel, M.; Offer, G. J.; Hinds, G.; Brett, D. J. L.; Shearing, P. R. In-operando high-speed tomography on lithium-ion batteries during thermal runaway. *Nat. Commun.* **2015**, *6*, 6924.
- (37) Yufit, V.; Shearing, P.; Hamilton, R. W.; Lee, P. D.; Wu, M.; Brandon, N. P. Investigation of lithium-ion polymer battery cell failure using X-ray computed tomography. *Electrochem. Commun.* **2011**, *13*, 608.

- (38) Ebner, M.; Geldmacher, F.; Marone, F.; Stampanoni, M.; Wood, V. X-ray Tomography of Porous, Transition Metal Oxide Based Lithium Ion Battery Electrodes. *Adv. Energy Mater.* **2013**, *3*, 845.
- (39) Tariq, F.; Yufit, V.; Kishimoto, M.; Shearing, P. R.; Menkin, S.; Golodnitsky, D.; Gelb, J.; Peled, E.; Brandon, N. P. Three-dimensional high resolution X-ray imaging and quantification of lithium ion battery mesocarbon microbead anodes. *J. Power Sources* **2014**, *248*, 1014.
- (40) Shearing, P. R.; Brandon, N. P.; Gelb, J.; Bradley, R.; Withers, P. J.; Marquis, A. J.; Cooper, S.; Harris, S. J. Multi Length Scale Microstructural Investigations of a Commercially Available Li-Ion Battery Electrode. *J. Electrochem. Soc.* **2012**, *159*, A1023.
- (41) Müller, S.; Pietsch, P.; Brandt, B.-E.; Baade, P.; De Andrade, V.; De Carlo, F.; Wood, V. Quantification and modeling of mechanical degradation in lithium-ion batteries based on nanoscale imaging. *Nat. Commun.* **2018**, *9*, 2340.
- (42) Ebner, M.; Chung, D.-W.; García, R. E.; Wood, V. Tortuosity Anisotropy in Lithium-Ion Battery Electrodes. *Adv. Energy Mater.* **2014**, *4*, 1301278.
- (43) Ebner, M.; Wood, V. Tool for Tortuosity Estimation in Lithium Ion Battery Porous Electrodes. *J. Electrochem. Soc.* **2015**, *162*, A3064.
- (44) Yang, F.; Liu, Y.; Martha, S. K.; Wu, Z.; Andrews, J. C.; Ice, G. E.; Pianetta, P.; Nanda, J. Nanoscale Morphological and Chemical Changes of High Voltage Lithium-Manganese Rich NMC Composite Cathodes with Cycling. *Nano Lett.* **2014**, *14*, 4334.
- (45) Pietsch, P.; Westhoff, D.; Feinauer, J.; Eller, J.; Marone, F.; Stampanoni, M.; Schmidt, V.; Wood, V. Quantifying microstructural dynamics and electrochemical activity of graphite and silicon-graphite lithium ion battery anodes. *Nat. Commun.* **2016**, *7*, 12909.
- (46) Ebner, M.; Marone, F.; Stampanoni, M.; Wood, V. Visualization and quantification of electrochemical and mechanical degradation of Li ion batteries. *Science* **2013**, *342*, 716.
- (47) Tariq, F.; Yufit, V.; Eastwood, D. S.; Merla, Y.; Biton, M.; Wu, B.; Chen, Z.; Freedman, K.; Offer, G.; Peled, E.; Lee, P. D.; Golodnitsky, D.; Brandon, N. In-operando X-ray tomography study of lithiation induced delamination of Si based anodes for lithium-ion batteries. *ECS Electrochem. Lett.* **2014**, *3*, A76.
- (48) Finegan, D. P.; Darcy, E.; Keyser, M.; Tjaden, B.; Heenan, T. M. M.; Jervis, R.; Bailey, J. J.; Malik, R.; Vo, N. T.; Magdysyuk, O. V.; Atwood, R.; Drakopoulos, M.; DiMichiel, M.; Rack, A.; Hinds, G.; Brett, D. J. L.; Shearing, P. R. Characterising thermal runaway within lithium-ion cells by inducing and monitoring internal short circuits. *Energy Environ. Sci.* **2017**, *10*, 1377.
- (49) Osenberg, M.; Manke, I.; Hilger, A.; Kardjilov, N.; Banhart, J. An X-ray tomographic study of rechargeable Zn/MnO<sub>2</sub> batteries. *Materials* **2018**, *11*, 1486.
- (50) Arlt, T.; Schröder, D.; Krewer, U.; Manke, I. In operando monitoring of the state of charge and species distribution in zinc air batteries using X-ray tomography and model-based simulations. *Phys. Chem. Chem. Phys.* **2014**, *16*, 22273.
- (51) Schmitt, T.; Arlt, T.; Manke, I.; Latz, A.; Horstmann, B. Zinc electrode shape-change in secondary air batteries: A 2D modeling approach. *J. Power Sources* **2019**, *432*, 119.
- (52) Schröder, D.; Arlt, T.; Krewer, U.; Manke, I. Analyzing transport paths in the air electrode of a zinc air battery using X-ray tomography. *Electrochem. Commun.* **2014**, *40*, 88.
- (53) Franke-Lang, R.; Arlt, T.; Manke, I.; Kowal, J. X-ray tomography as a powerful method for zinc-air battery research. *J. Power Sources* **2017**, *370*, 45.
- (54) Christensen, M. K.; Mathiesen, J. K.; Simonsen, S. B.; Norby, P.; Norby, P. Transformation and migration in secondary zinc-air batteries studied by in situ synchrotron X-ray diffraction and X-ray tomography. *J. Mater. Chem. A* **2019**, *7*, 6459.
- (55) Titscher, P.; Helmers, L.; Diener, A.; Kwade, A. Deposition of Zinc Species in 3D Structured Zinc Anodes in Nonstirred Alkaline Systems Observed by X-Ray Micro Tomography. *Energy Technol.* **2019**, *7*, 1900234.
- (56) Bozzini, B.; Altissimo, M.; Amati, M.; Bocchetta, P.; Gianoncelli, A.; Gregoratti, L.; Kourousias, G.; Mancini, L.; Mele, C.; Kiskinova, M. In Situ and Ex Situ X-Ray Microspectroelectrochemical Methods for the Study of Zinc-Air Batteries. In *Elsevier Reference Module in Chemistry, Molecular Sciences and Chemical Engineering*; Reedijk, J., Ed.; Elsevier: Waltham, 2015; p 1.
- (57) Yufit, V.; Tariq, F.; Eastwood, D. S.; Biton, M.; Wu, B.; Lee, P. D.; Brandon, N. P. Operando visualization and multi-scale tomography studies of dendrite formation and dissolution in zinc batteries. *Joule* **2019**, *3*, 485.
- (58) Zandomenighi, D.; Voltolini, M.; Mancini, L.; Brun, F.; Dreossi, D.; Polacci, M. Quantitative analysis of X-ray microtomography images of geomaterials: Application to volcanic rocks. *Geosphere* **2010**, *6*, 793.
- (59) Wilkins, S. W.; Gureyev, T. E.; Gao, D.; Pogany, A.; Stevenson, A. W. Phase-contrast imaging using polychromatic hard X-rays. *Nature* **1996**, *384*, 335.
- (60) Feldkamp, L. A.; Davis, L. C.; Kress, J. W. Practical cone-beam algorithm. *J. Opt. Soc. Am. A* **1984**, *1*, 612.
- (61) Schindelin, J.; Arganda-Carreras, I.; Frise, E.; Kaynig, V.; Longair, M.; Pietzsch, T.; Preibisch, S.; Rueden, C.; Saalfeld, S.; Schmid, B.; Tinevez, J.-Y.; White, D. J.; Hartenstein, V.; Eliceiri, K.; Tomancak, P.; Cardona, A. Fiji: an open-source platform for biological-image analysis. *Nat. Methods* **2012**, *9*, 676.
- (62) Brun, F.; Mancini, L.; Kasae, P.; Favretto, S.; Dreossi, D.; Tromba, G. Pore3D: A software library for quantitative analysis of porous media. *Nucl. Instrum. Methods Phys. Res., Sect. A* **2010**, *615*, 326.
- (63) Brun, F.; Kourousias, G.; Dreossi, D.; Mancini, L. An improved method for ring artifacts removing in reconstructed tomographic images. *World Congress on Medical Physics and Biomedical Engineering, September 7–12, 2009, Munich, Germany*; Springer: Berlin, Heidelberg, 2009; pp 926–929.
- (64) Otsu, N. A threshold selection method from gray-level histograms. *IEEE Trans. Syst. Man Cybern.* **1979**, *9*, 62.
- (65) Chen, S.; Haralick, R. M. Recursive erosion, dilation, opening, and closing transforms. *IEEE Trans. Image Process.* **1995**, *4*, 335.
- (66) Hartigan, J. A.; Wong, M. A. Algorithm AS 136: A k-means clustering algorithm. *Appl. Stat.* **1979**, *28*, 100.
- (67) Arzilli, F.; Cilona, A.; Mancini, L.; Tondi, E. Using synchrotron X-ray microtomography to characterize the pore network of reservoir rocks: A case study on carbonates. *Adv. Water Resour.* **2016**, *95*, 254.
- (68) Lindquist, W. B.; Lee, S.-M.; Coker, D. A.; Jones, K. W.; Spanne, P. Medial axis analysis of void structure in three-dimensional tomographic images of porous media. *J. Geophys. Res.* **1996**, *101*, 8297.
- (69) Lee, T. C.; Kashyap, R. L.; Chu, C. N. Building skeleton models via 3-D medial surface axis thinning algorithms. *CVGIP Graph. Models Image Process.* **1994**, *56*, 462.
- (70) Hildebrand, T.; Rüegsegger, P. A new method for the model-independent assessment of thickness in three-dimensional images. *J. Microsc.* **1997**, *185*, 67.